

# **Wide modulation of coercive fields in Mn<sub>4</sub>N ferrimagnetic thin films caused dominantly by dislocation microstructures**

Shinji Isogami<sup>1\*</sup>, Mitsuru Ohtake<sup>2</sup>, Yusuke Kozuka<sup>1</sup>, and Yukiko K. Takahashi<sup>1</sup>

<sup>1</sup> Research Center for Magnetic and Spintronic Materials, National Institute for Materials Science, Sengen 1-2-1, Tsukuba, Ibaraki, 305-0047 Japan

<sup>2</sup> Faculty of Engineering, Yokohama National University, Tokiwadai 79-5, Hodogaya, Yokohama, Kanagawa, 240-8501 Japan

\*E-mail: isogami.shinji@nims.go.jp

**Perpendicular magnetic anisotropy and coercive fields ( $H_c$ ) are governed by the degree of order of N ( $S$ ) in ferrimagnetic Mn<sub>4</sub>N thin films. However, in this study, we observed non-negligible modulation of  $H_c$  extending from 10 to 7.5 kOe for three Mn<sub>4</sub>N films grown at a substrate temperature ( $T_{\text{sub}}$ ) in the range of 400–500 °C, even with identical  $S$ , which has not been discussed to date. The possible mechanisms for this phenomenon were explored by transport properties and fine structural analysis. The results indicated that longitudinal resistivity and anomalous Hall resistivity remain unchanged for three Mn<sub>4</sub>N films. Conversely, the number of**

dislocations and in-plane grain size ( $D$ ) increased, whereas the residual strain ( $\varepsilon$ ) decreased with increasing  $T_{\text{sub}}$ . This indicates that  $H_c$  of the  $\text{Mn}_4\text{N}$  film with the same  $S$  is sensitive to the variation in dislocations,  $D$  and  $\varepsilon$ . Tunable  $H_c$  of this type can be effectively applied in magnetic and spintronic devices using ferrimagnetic  $\text{Mn}_4\text{N}$  films, because  $H_c$  is an important determinant of the thermal stability of magnetization and working power consumption.

## Keywords

Coercive field, Dislocation, Microstructure,  $\text{Mn}_4\text{N}$

## <Main text>

### I. Introduction

Uniaxial magnetic anisotropy energy density ( $K_u$ ) and saturation magnetization ( $M_s$ ) for magnetic thin films are responsible for the efficiency of current-induced magnetization switching in recent spintronic applications such as magnetic random access memories,<sup>1-4</sup> in which various magnetic thin films have been employed. In particular, for Mn-based nitride thin films with antiperovskite structure, several magnetic structures have been revealed to date, which are non-collinear antiferromagnetism for  $\text{Mn}_3\text{XN}$  (X: transition metals)<sup>5,6</sup> and collinear ferrimagnetism for 001-oriented

Mn<sub>4</sub>N films with perpendicular magnetic anisotropy (PMA).<sup>7-12</sup> In contrast to these films, the dominant magnetic structures for the different 111-oriented Mn<sub>4</sub>N films are non-collinear,<sup>13-17</sup> and the possible magnetic compensation and related phenomena are studied in MnXN thin films.<sup>18-21</sup>

These magnetic structures are strongly affected by the atomic-site ordering of N at the body-centered site (*S*) in the antiperovskite unit cell; therefore, PMA for the 001-oriented Mn<sub>4</sub>N films with a magnetic easy axis pointing perpendicular to the film plane suppressed in the case of *S* far from the maximum value.<sup>11,12</sup> This may be applicable to alloy thin films with PMA such as FePt,<sup>22</sup> MnAl,<sup>23</sup> and MnGa.<sup>24</sup> However, we have also found an additional issue from the previous study that non-negligible deviation of coercive field ( $H_c$ ) is observed in the 001-oriented Mn<sub>4</sub>N films regardless of the *S* near maximum values in the experiments.<sup>25</sup> In addition, some reports show the different size of  $H_c$  depending on the substrates and fabrication techniques, such as molecular beam epitaxy and sputtering.<sup>10,11,26</sup> Although the mechanisms of various  $H_c$  are extensively investigated in numerous bulks and thin films to date except for the Mn<sub>4</sub>N films,<sup>27-31</sup> there has been no focus on which factors contribute to  $H_c$  sensitively, in the case of specific Mn<sub>4</sub>N thin films.

Understanding the variation of  $H_c$  in the Mn<sub>4</sub>N ferrimagnetic thin films with maximum *S* leads to an efficient tunability of  $H_c$ , which is indispensable for Mn<sub>4</sub>N films to realize advanced spintronic devices. For example, the enhanced  $H_c$  can provide thermal stability without bias fields, resulting in a reliable thermal-flux sensor based on the anomalous Nernst effect,<sup>32</sup> and the suppression of  $H_c$  can

reduce the magnetic switching barrier, resulting in a low critical current density for magnetic memory.<sup>1-4</sup> In addition, skyrmion bubbles and their related topological Hall effects are observed in Mn<sub>4</sub>N films,<sup>33-37</sup> such that the  $H_c$  fine-control technology can realize future skyrmionic quantum storage systems.<sup>38</sup>

The present study aims to identify the key factors that determine the deviation of  $H_c$  for 001-oriented Mn<sub>4</sub>N films with maximum  $S$ . Three Mn<sub>4</sub>N films were prepared at three different substrate temperatures ( $T_{\text{sub}}$ ), all of which have almost the same  $S$ . Structural analysis and the magnetic and transport properties of the films were examined. As a result,  $H_c$  was sensitive to grain diameter, microstructure, and strain, which were not detectable by X-ray diffractometry (XRD). Finally, we discuss technology for controlling  $H_c$  in ferrimagnetic Mn<sub>4</sub>N films.

## II. Experimental procedures

Thin films of 25-nm-thick Mn<sub>4</sub>N were deposited on a single-crystal 100-MgO substrate via reactive nitridation sputtering. Three  $T_{\text{sub}}$  were employed: 400, 450, and 500 °C. The flow rate of N<sub>2</sub> to Ar gas were in the ratio of 16%. Structural analysis was performed using XRD with Cu  $K\alpha$  radiation (SmartLab, Rigaku Corporation, Tokyo, Japan) and transmission electron microscopy (TEM) (Titan G2 80-200, FEI Company (Thermo Fisher Scientific), Oregon, USA). The surface roughness ( $R_a$ ) and morphology were observed via atomic force microscopy (AFM) (SPA400, SII Nano Technology Inc., Tokyo, Japan). Magnetic properties were measured using a vibrating sample

magnetometer (VSM; VSM 8600 series, Lake Shore Cryotronics, Inc., Ohio, USA) at room temperature. The  $K_u$  was determined using the saturation torque amplitudes, where the external magnetic field rotates out-of-plane.<sup>39</sup>

### III. Results and discussions

#### A. Characterization of Mn<sub>4</sub>N crystal structures

Figure 1(a) shows the out-of-plane XRD profiles of the Mn<sub>4</sub>N films fabricated at  $T_{\text{sub}}$  values of 400, 450, and 500 °C (red, black, and blue, respectively). The peaks at  $2\theta/\omega \approx 23^\circ$  and  $47^\circ$  indicate diffraction from Mn<sub>4</sub>N 001 and 002, respectively. Such diffraction angles were consistent for the three samples, suggesting no significant change in the out-of-plane lattice constant, regardless of the different  $T_{\text{sub}}$ . These results were applicable to in-plane XRD, as shown in Fig. 1(b); that is, the in-plane lattice constants were independent of  $T_{\text{sub}}$ . The Mn-O indicates natural oxidation layers because the diffraction peaks of Mn-O at  $2\theta/\omega \approx 41^\circ$  were predominant for the in-plane XRD compared with those for the out-of-plane XRD, and the presence of Mn-O natural oxidation layer has been identified by our previous study with cross-sectional TEM observation.<sup>12</sup> The inset of Fig. 1(c) represents the Mn<sub>4</sub>N unit cell, in which the directions of magnetic moments alternate along the [001] direction, resulting in the ferrimagnetic order with PMA.<sup>12</sup> The  $c/a$  was estimated to be  $\sim 0.989$  for all samples, which is the typical value for Mn<sub>4</sub>N films with sizable PMA.<sup>10-12</sup> Judging from the results that no diffraction peaks were observed in the grazing incidence XRD, the present Mn<sub>4</sub>N films formed a strong

(001) fiber sheet texture without any polycrystals. The full-width at half-maximum of the rocking curves ( $\Delta\omega_{1/2}$ ) showed similar values for all samples, suggesting that the deviation in the crystal orientation was comparable for all samples or slightly increased with increasing  $T_{\text{sub}}$  [Fig. 1(d)]. These results show that the variation in crystal structures depending on  $T_{\text{sub}}$  was not clearly detected by XRD analysis.

## B. Non-negligible coercivity deviation for Mn<sub>4</sub>N films

Figure 2(a) shows the  $M$ - $H$  (magnetization - field) hysteresis loops for the Mn<sub>4</sub>N films fabricated with three different  $T_{\text{sub}}$ . The  $M_s$  was similar for the three samples, as shown in Fig. 2(b), whereas the non-negligible variation of  $H_c$  was evident:  $H_c \approx 10$  kOe (7.5 kOe) for  $T_{\text{sub}} = 400$  °C (500 °C), that is,  $H_c$  was suppressed by higher  $T_{\text{sub}}$ . Figure 2(c) shows the  $K_u$  for three samples measured via the anomalous Hall effects while rotating the external field in the  $yz$ -plane, as shown in the inset,<sup>39</sup> The coherent magnetization rotation model being considered,  $H_c$  should be comparable to the anisotropy field ( $H_k$ ), which is expressed as  $H_c \approx H_k = 2K_u/M_s$ ; therefore, the deviation of  $H_c$  observed in this study cannot be explained by either  $K_u$  or  $M_s$ . To address this point quantitatively, the measured  $H_c$  for the three samples was compared with the  $H_k$  (estimated by  $2K_u/M_s$  using the measured  $K_u$  and  $M_s$ ) [Fig. 2(d)]. As a result, the  $H_c$  was smaller by ~40% (~60%) for  $T_{\text{sub}} = 400$  °C (500 °C) than  $H_k$ . These results can be explained by the domain nucleation mechanism prior to coherent rotation. Figure 2(d) also shows the variation in  $H_c$  and  $H_k$  normalized by those for  $T_{\text{sub}} = 400$  °C. More

importantly, the decrease in  $H_c$  by 26% was more tangible compared with the decrease in  $H_k$  by 4% with increasing  $T_{\text{sub}}$ , suggesting the superposition of different suppression mechanisms from the domain nucleation. To explore the possible mechanisms that cause such suppression of  $H_c$  with increasing  $T_{\text{sub}}$ , the three samples were systematically investigated in terms of the crystal microstructure, morphology, and transport properties.

### C. Grain diameter and strain estimated from XRD profiles

Figure 3(a) shows the in-plane grain diameter ( $D_{\text{grain}}$ ) estimated using Scherrer's formula:<sup>40</sup>  $D = K\lambda/\beta\cos\theta$ , where the constant  $K = 0.94$  was employed because the diffraction peak from  $\text{Mn}_4\text{N}$  200 was fitted by a Gaussian function,  $\lambda$  is the wavelength of Cu  $K_\alpha$  radiation (0.154 nm),  $\beta$  is the full width at half maximum of the peak, and  $\theta$  is the diffraction angle of  $\text{Mn}_4\text{N}$  200 in the in-plane XRD profiles [Fig. 1(b)]. Although the difference was not significant, an increase in  $D_{\text{grain}}$  was evident with increasing  $T_{\text{sub}}$ , suggesting grain growth of  $\text{Mn}_4\text{N}$  with increasing  $T_{\text{sub}}$ , as confirmed in the AFM images [see insets of Fig. 3(a)]. The  $R_a$  also increased with increasing  $T_{\text{sub}}$ , which can be attributed to the grain growth of  $\text{Mn}_4\text{N}$ . This may be due to the nature of the metallic films fabricated at high  $T_{\text{sub}}$  values. In addition to the trend of  $D_{\text{grain}}$ , Fig. 3(b) shows the strain ( $\varepsilon$ ) estimated using the formula  $\varepsilon = \beta/4\tan\theta$ . The largest  $\varepsilon$  of ~0.465% was obtained for  $T_{\text{sub}} = 400$  °C, suggesting the tensile strain, which decreased with increasing  $T_{\text{sub}}$ . Although the  $T_{\text{sub}}$ -dependent variation of  $\varepsilon$  was approximately 5% of the  $\varepsilon$  for  $T_{\text{sub}} = 400$  °C, the variation should be accounted for as a candidate to affect  $H_c$ , in terms of

the prediction that strain gives rise to a significant magnetic frustration in the Mn-based antiperovskite nitrides such as  $\text{Mn}_3\text{XN}$ .<sup>41</sup>

#### **D. Undetectable microstructures via XRD**

Figure 4(a1) shows a cross-sectional annular dark-field scanning transmission electron microscopy (ADF-STEM) image of the  $\text{Mn}_4\text{N}$  film fabricated at  $T_{\text{sub}} = 400$  °C, with the largest  $H_c$  of 10 kOe. The inset shows a representative electron diffraction pattern for a large part of the  $\text{Mn}_4\text{N}$  film, that is, the diffraction pattern does not indicate the local but the averaged (corresponding to the area with 10  $\mu\text{m}$  width of this STEM image) crystal structures. The appearance of inhomogeneous contrast in the STEM image was consistent with the previous report of  $\text{Mn}_4\text{N}$  films fabricated using a facing-target sputtering technique.<sup>42</sup> Such nonuniform microstructures are widely known as Moire fringes that appear when two or more crystal lattices are interfered with.<sup>43</sup> Therefore, it is inferred that the present  $\text{Mn}_4\text{N}$  film may involve grains with both tiny lattice distortions and rotations. The diffraction pattern exhibited clear spots originating from the 002 fundamental lattice and 001 superlattice, which is consistent with the XRD profiles [Figs. 1(a) and 1(b)]. These characteristics were also observed for  $T_{\text{sub}} = 450$  °C and 500 °C [Figs. 4(b1) and 4(c1)], that is, both STEM images exhibited inhomogeneous contrast, and the diffraction patterns exhibited clear spots originating from the 002 fundamental lattice and 001 superlattice.

To explore the possible microstructure mechanisms, we studied high-resolution STEM images

[Fig. 4(a2)]. The substrate/film interface is depicted by a yellow dashed line. A flat and smooth layer with uniform contrast can be seen near the interface, suggesting coherent growth of the initial two or three monolayers of  $\text{Mn}_4\text{N}$ . Figure 4(a3) shows the Fourier-filtered STEM image in Fig. 4(a2). Dislocations were observed on the top of the initial growth layer. They play a role in relaxing the substrate-induced stress because the in-plane lattice mismatch was larger by as much as 10% between  $\text{MgO}$  and  $\text{Mn}_4\text{N}$ .<sup>44</sup> Note that the dislocation sites agreed with those with bright contrast, which originates from the Moire fringe mentioned above, in the high-resolution STEM image, as indicated by arrows with the same length in both Figs. 4(a2) and 4(a3). These results show that the dislocations nucleate predominantly where the  $\text{Mn}_4\text{N}$  grains are adjacent to those with different lattice constants and directions. Except for the in-plane dislocation near the substrate/film interface, no dislocations were observed at the middle level of the film, although an inhomogeneous contrast was still observed in the corresponding part of the film [Fig. 4(a2)]. This may be because the strain may not be too strong to nucleate any dislocations. This growth mode is reasonable in the films with mismatches as large as 10%, and we reported the same nature in the  $\text{Fe}_4\text{N}$  film on a  $\text{MgO}$  substrate, the same family of antiperovskite nitrides as  $\text{Mn}_4\text{N}$ .<sup>44</sup>

In contrast to the film with  $T_{\text{sub}} = 400$  °C, the microstructures exhibited a remarkable change at higher  $T_{\text{sub}}$  values. Figures 4(b2) and 4(b3) show the high-resolution STEM image and Fourier-filtered STEM image for  $T_{\text{sub}} = 450$  °C. Whereas the Moire fringe was still observed [Fig. 4(b2)], as

in the case for  $T_{\text{sub}} = 400$  °C, many dislocations nucleated at sites far from the substrate compared with those near the substrate/film interface [Fig. 4(b3)]. Possible interpretations to be considered are: Larger strain could be expected compared with the case of lower  $T_{\text{sub}}$ , considering the thermal expansion coefficient of MgO;<sup>45</sup> such strain was introduced up to the middle level of the film with less dislocations owing to the thermal effect, followed by nucleation of dislocation remarkably occurred, which was never found in the film for  $T_{\text{sub}} = 400$  °C. These results were applicable for the case of  $T_{\text{sub}} = 500$  °C [Figs. 4(c2) and 4(c3)], that is, overall, the microstructures for  $T_{\text{sub}} = 500$  °C can be explained by a scenario similar to those for  $T_{\text{sub}} = 450$  °C. This feature might be in agreement with the non-linear variation of  $D_{\text{grain}}$ ,  $\varepsilon$ , and even magnetic properties against  $T_{\text{sub}}$ : A large (relatively small) variation was observed at  $T_{\text{sub}}$  between 400–450 °C (450–500 °C) (Figs. 3).

### **E. Influences on the longitudinal and transverse resistivity**

To study the effect of  $T_{\text{sub}}$  on the electron transport properties, we measured both the longitudinal ( $\rho_{xx}$ ) and transverse resistivity ( $\rho_{xy}$ ) of Mn<sub>4</sub>N films fabricated with three different  $T_{\text{sub}}$ . Figures 5(a) and 5(b) show  $\rho_{xx}$  and  $\rho_{xy}$ , respectively, as a function of the measurement temperature ( $T$ ). Consistent with previous results, both  $\rho_{xx}$  and  $\rho_{xy}$  decreased with decreasing  $T$ .<sup>37</sup> The film for  $T_{\text{sub}} = 400$  °C showed a slightly smaller value compared with the other two samples. We consider that such a small discrepancy can be ignored, which is supported by the relationship between the transverse ( $\sigma_{xy}$ ) and longitudinal conductivity ( $\sigma_{xx}$ ), that is, the three films agree with each other [Fig. 5(c)]. Because

the  $\sigma_{xy}$  showed almost constant values at approximately  $\sigma_{xx} \approx 10^4$  S/cm, it was inferred that the  $\sigma_{xy}$  for the films could be dominated by an intrinsic rather than extrinsic origin.<sup>46</sup> Figure 5(d) shows the dependences of  $\rho_{xx}^0$  and  $\rho_{xy}^0$  on  $T_{\text{sub}}$  at 5 K, which corresponds to the values eliminating the contributions from phonons. Clear  $T_{\text{sub}}$  dependences cannot be observed for either value, suggesting that the different microstructures of the three Mn<sub>4</sub>N films did not play a significant role in varying the transport properties.

To discuss the dominant influential factors on  $H_c$  in the case of ferrimagnetic Mn<sub>4</sub>N films with the maximum  $S$ , experimental data were replotted against  $H_c$ , as shown in Fig. 6. We categorized these results into four contribution types: the averaged crystal structure evaluated via XRD [Figs. 6(a) and 6(b)], surface roughness [Fig. 6(c)], microstructure [Figs. 6(d) and 6(e)], and transport properties [Fig. 6(f)]. As a result, it was revealed that the  $S$ ,  $\Delta\omega_{1/2}$ , and electronic transport properties do not significantly contribute to  $H_c$ , whereas the surface roughness and microstructure are the keys to modulating  $H_c$  in ferrimagnetic Mn<sub>4</sub>N films. Therefore, we have eliminated the  $S$ ,  $\Delta\omega_{1/2}$ , and electronic transport properties from our discussion. A small  $D_{\text{grain}}$  was responsible for the decreased  $R_a$ , resulting in the enhancement of  $H_c$ . To understand this point first, we consider the Stoner-Wohlfarth model without magnetic interaction, given by the following formula:<sup>30</sup>

$$\begin{aligned}
 H_c &= 0.482 \frac{2K_u}{\mu_0 M_s} \\
 &= 0.482 \left( \frac{2K_1}{\mu_0 M_s} + \frac{1-3N}{2} M_s \right), \quad (1)
 \end{aligned}$$

where  $K_u$ ,  $\mu_0$ ,  $M_s$ ,  $K_1$ , and  $N$  represent the uniaxial magnetic anisotropy energy density, vacuum permeability, saturation magnetization, magnetocrystalline anisotropy energy density, and demagnetization factor, respectively, ranging from 0 to 1. Because  $K_1$  and  $M_s$  were independent of  $T_{\text{sub}}$ , judging from our experiments (Fig. 2), one of the factors that gives a different  $H_c$  is the  $N$  in the film. Therefore, Eq. (1) suggests that the enhancement of  $H_c$  can be qualitatively understood by the decrease in  $N$  when  $D_{\text{grain}}$  decreases with a lower  $T_{\text{sub}}$ . Although the realistic value of  $N$  for each  $\text{Mn}_4\text{N}$  film is still unknown in this study, this trend is consistent with the statement by Liu *et al.* that the local demagnetization factor decreases as the grain size is decreased.<sup>31</sup> However, the contribution from the demagnetization factor [the second term of Eq. (1)] is not large enough to explain the variation in measured  $H_c$  with 26% against  $T_{\text{sub}}$  [Fig. 2(d)] because the variation in estimated  $H_c$  is only 10% with  $N = 0$  and 1. Next, we consider  $\varepsilon$  to have an additional effect on  $H_c$ . Stress-induced enhancement of  $H_c$  by 300% was demonstrated in a ferrimagnetic amorphous TbFeCo thin film with PMA by Anuniwat *et al.*<sup>28</sup> In the case of  $\text{Mn}_4\text{N}$  films, it was revealed that the number of dislocations was enhanced with higher  $T_{\text{sub}}$  (Fig. 4), resulting in the suppression of  $\varepsilon$  with higher  $T_{\text{sub}}$  [Fig. 3(b)]. Therefore, the enhancement of  $H_c$  in  $\text{Mn}_4\text{N}$  films with a lower  $T_{\text{sub}}$  is also associated with the enhancement of  $\varepsilon$ . These results lead us to conclude that the variation in the measured  $H_c$  depending on  $T_{\text{sub}}$  in the  $\text{Mn}_4\text{N}$  films could be dominantly affected by the combined classical mechanisms of ferromagnets and/or ferrimagnets, which are demagnetization factors determined by the grain size and the effective residual

strain with dislocations.

The  $H_c$  for the optimum  $Mn_4N$  films with the maximum  $S$  was found to be sensitive to the grain size and strain as a result of a specific substrate temperature. Such tunable  $H_c$  is an attractive phenomenon from the perspective of magnetic and spintronic devices: Thermal stability can be improved by a large  $H_c$  without bias fields and reduction of working power consumption by a small  $H_c$ . In addition, the size of skyrmion bubbles can be manipulated without a bias field. The technology to tune  $H_c$  could thus promote  $Mn_4N$  based spintronic devices in the future.

#### **IV. Conclusion**

It is already known that the  $H_c$  of  $Mn_4N$  ferrimagnetic thin films is strongly governed by their degree of order of N. This is due to the strong correlation between the degree of order of N and PMA. Namely, the out-of-optimization content of N as well as  $T_{sub}$  causes less degree of order of N and decrease in PMA, resulting in small  $H_c$ , which might be general characteristics for magnetic nitrides. However, this study specifically focused on the property of  $H_c$  that could be modulated by dislocations as well as microstructures with similar  $S$ , which has not previously been examined in detail via TEM observation. Neither the deviation of crystal orientation nor the longitudinal and transverse resistivity contribute significantly to  $H_c$ ; however, it is sensitive to the demagnetization factor, determined by the grain size and the effective residual strain with dislocations. This type of tunability of  $H_c$  is an intriguing characteristic of  $Mn_4N$  films with a maximum degree of order of N.

The results demonstrate that decreasing or increasing the grain size and number of dislocations via optimization of the substrate temperature and/or lattice mismatch between the substrate and film is a promising method to enhance or suppress  $H_c$ .

### **<Acknowledgement>**

This work was supported by KAKENHI Grants-in-Aid (Nos. 18H03787 and 19K04499) from the Japan Society for the Promotion of Science (JSPS). Part of this work was carried out under the Cooperative Research Project Program of RIEC, Tohoku University.

### **<Data Availability>**

The data supporting the findings of this study are available from the corresponding author upon reasonable request.

### **<Conflict interest>**

The authors have no conflict of interests to declare.

## <References>

- [1] C. Slonczewski, *J. Magn. Magn. Mater.* 159, L1 (1996).
- [2] L. Berger, *J. Appl. Phys.* 55, 1954 (1984).
- [3] R. H. Koch, J. A. Katine, and J. Z. Sun, *Phys. Rev. Lett.* 92, 088302 (2004).
- [4] S. Ikeda, K. Miura, H. Yamamoto, K. Mizunuma, H. D. Gan, M. Endo, S. Kanai, J. Hayakawa, F. Matsukura, and H. Ohno, *Nature Mater.* 9, 721 (2010).
- [5] X. Zhou, J.-P. Hanke, W. Feng, F. Li, G.-Y. Guo, Y. Yao, S. Blügel, and Y. Mokrousov, *Phys. Rev. B* 99, 104428 (2019).
- [6] V. T. N. Huyen, M. Suzuki, K. Yamauchi, and T. Oguchi, *Phys. Rev. B* 100, 094426 (2019).
- [7] W. J. Takei, G. Shirane, and B. C. Frazer, *Phys. Rev.* 119, 1893 (1960).
- [8] W. J. Takei, R. R. Heikes, and G. Shirane, *Phys. Rev.* 125, 1893 (1962).
- [9] K. M. Ching, W. D. Chang, T. S. Chin, J. G. Duh, and H. C. Ku, *J. Appl. Phys.* 76, 6582 (1994).
- [10] Y. Yasutomi, K. Ito, T. Sanai, K. Toko, and T. Suemasu, *J. Appl. Phys.* 115, 17A935 (2014).
- [11] K. Kabara, and M. Tsunoda, *J. Appl. Phys.* 117, 17B512 (2015).

- [12] S. Isogami, K. Masuda, and Y. Miura, *Phys. Rev. Mater.* 4, 014406 (2020).
- [13] M. Uhl, S. Matar, and P. Mohn, *Phys. Rev. B* 55, 2995 (1997).
- [14] S. Dhar, O. Brandt, and K. H. Ploog, *Appl. Phys. Lett.* 86, 112504 (2005).
- [15] Z. Zhang, Y. Cho, J. Singhal, X. Li, P. Dang, H. Lee, J. Casamento, Y. Tang, H. G. Xing, and D. Jena, *AIP Adv.* 10, 015238 (2020).
- [16] Z. Zhang, Y. Cho, M. Gong, S.-T. Ho, J. Singhal, J. Encomendero, X. Li, H. Lee, H. G. Xing, and D. Jena, *IEEE Trans. Magn.* 58, 2400106 (2021).
- [17] S. Isogami, N. Rajamanickam, Y. Kozuka, and Y. K. Takahashi, *AIP Adv.* 11, 105314 (2021).
- [18] S. Isogami, A. Anzai, T. Gushi, T. Komori, and T. Suemasu, *Jpn. J. Appl. Phys.* 57, 120305 (2018).
- [19] T. Komori, T. Gushi, A. Anzai, L. Vila, J.-P. Attane, S. Pizzini, J. Vogel, S. Isogami, K. Toko, and T. Suemasu, *J. Appl. Phys.* 125, 213902 (2019).
- [20] H. Mitarai, T. Komori, T. Hirose, K. Ito, S. Ghosh, S. Honda, K. Toko, L. Vila, J.-P. Attané, K. Amemiya, and T. Suemasu, *Phys. Rev. Mater.* 4, 094401 (2020).

- [21] T. Komori, T. Hirose, T. Gushi, K. Toko, T. Hanashima, L. Vila, J.-P. Attane, K. Amemiya, and T. Suemasu, *J. Appl. Phys.* 127, 043903 (2020).
- [22] M. R. Visokaya, and R. Sinclair, *Appl. Phys. Lett.* 66, 1692 (1995).
- [23] T. Sands, J. P. Harbison, M. L. Leadbeater, S. J. Allen, Jr., G. W. Hull, R. Ramesh, and V. G. Keramidas, *Appl. Phys. Lett.* 57, 2609 (1990).
- [24] H. Kurt, K. Rode, M. Venkatesan, P. Stamenov, and J. M. D. Coey, *Phys. Rev. B* 83, 020405(R) (2011).
- [25] S. Isogami, K. Masuda, Y. Miura, N. Rajamanickam, and Y. Sakuraba, *Appl. Phys. Lett.* 118, 092407 (2021).
- [26] T Gushi, L. Vila, O. Fruchart, A. Marty, S. Pizzini, J. Vogel, F. Takata, A. Anzai, K. Toko, T. Suemasu, and J.-P. Attané, *Jpn. J. Appl. Phys.* 57, 120310 (2018).
- [27] W. B. Cui, Y. K. Takahashi, K. Hono, *Acta Mater.* 59, 7768 (2011).
- [28] N. Anuniwat, M. Ding, S. J. Poon, S. A. Wolf, and J. Lu, *J. Appl. Phys.* 113, 043905 (2013).
- [29] H. Sepehri-Amin, T. Phkubo, M. Gruber, T. Schrefl, and K. Hono, *Scripta Mater.* 89, 29 (2014).

- [30] Y. Takahashi, T. Kadono, S. Yamamoto, V. R. Singh, V. K. Verma, K. Ishigami, G. Shibata, T. Harano, Y. Takeda, T. Okane, Y. Saitoh, H. Yamagami, M. Takano, and A. Fujimori, *Phys. Rev. B* 90, 024423 (2014).
- [31] J. Liu, H. Sepehri-Amin, T. Ohkubo, K. Hioki, A. Hattori, T. Schrefl, and K. Hono, *Acta Mater.* 82, 336 (2015).
- [32] W. Zhou and Y. Sakuraba, *Appl. Phys. Express* 13, 043001 (2020).
- [33] G. Wang, S. Wu, W. Zhou, H. Li, D. Li, T. Dai, S. Kang, S. Dang, X. Ma, P. Hu, and S. Li, *Appl. Phys. Lett.* 113, 144403 (2018).
- [34] M. Meng, S. Li, M. Saghayezhian, E. W. Plummer, and R. Jin, *Appl. Phys. Lett.* 112, 132402 (2018).
- [35] C. Ma, T. Hartnett, W. Zhou, P. Balachandran, and S. Poon, *Appl. Phys. Lett.* 119, 192406 (2021).
- [36] T. Bayaraa, C. Xu, and L. Bellaiche, *Phys. Rev. Lett.* 127, 217204 (2021).
- [37] S. Isogami, M. Ohtake, and Y. K. Takahashi, *J. Appl. Phys.* 131, 073904 (2022).

- [38] S. Luo, and L. You, *APL Mater.* 9, 050901 (2021).
- [39] T. Ono, N. Kikuchi, S. Okamoto, O. Kitakami, and T. Shimatsu, *Appl. Phys. Express* 11, 033002 (2018).
- [40] Scherrer, P., *Nachr. Ges. Wiss. Göttingen*, 26, 98 (1918).
- [41] J. Zemen, E. Mendive-Tapia, Z. GerCSI, R. Banerjee, J. B. Staunton, and K. G. Sandeman, *Phys. Rev. B* 95, 184438 (2017).
- [42] Z. Zhang, X. Shi, X. Liu, X. Chen, and W. Mi, *J. Phys.: Condens. Mater.* 34, 065802 (2022).
- [43] Q. H. Wang, S. Ri, H. Tsuda, M. Kodera, K. Suguro, and N. Miyashita, *Nanotechnology* 28, 455704 (2017).
- [44] I. Suzuki, J. Uzuhashi, T. Ohkubo, and S. Isogami, *Mater. Res. Express* 6, 106446 (2019).
- [45] M. A. Durand, *Physics*, 7, 297 (1936).
- [46] S. Onoda, N. Sugimoto, and N. Nagaosa, *Phys. Rev. B* 77, 165103 (2008).

### <Figure captions>

**Figure 1.** (a) Out-of-plane, (b) in-plane, and (c) grazing incidence x-ray diffraction (XRD) profiles for the Mn<sub>4</sub>N films fabricated with the substrate temperature ( $T_{\text{sub}}$ ) of 400 °C (red), 450 °C (black), and 500 °C (blue). Inset of Fig. 1(c) represents the Mn<sub>4</sub>N unit cell with collinear ferrimagnetic magnetic structure. (d) Full-width at half-maximum value ( $\Delta\omega_{1/2}$ ) as a function of  $T_{\text{sub}}$ , where  $\Delta\omega_{1/2}$  was estimated from the rocking curves of XRD as shown in the inset.

**Figure 2.** (a) Magnetization-field ( $M$ - $H$ ) hysteresis loops for the Mn<sub>4</sub>N films fabricated with the substrate temperature ( $T_{\text{sub}}$ ) of 400 °C (red), 450 °C (black), and 500 °C (blue). (b)  $T_{\text{sub}}$  dependence of saturation magnetization ( $M_s$ ), (c) uniaxial magnetic anisotropy energy density ( $K_u$ ) that is estimated from the angular dependence of anomalous Hall effect, and (d) coercive field ( $H_c$ ) and anisotropy field ( $H_k = 2K_u/M_s$ ).

**Figure 3.** (a)  $T_{\text{sub}}$  dependence of the in-plane grain diameter ( $D_{\text{grain}}$ ) and (b) residual strain ( $\varepsilon$ ) evaluated using XRD profiles. Surface morphologies observed via atomic force microscopy (AFM) are shown in the insets.

**Figure 4.** (a1) Cross sectional annular dark-field scanning transmission electron microscopy (ADF-STEM) image, (a2) enlarged ADF-STEM image, and (a3) Fourier filtered image for the Mn<sub>4</sub>N film fabricated with the substrate temperature ( $T_{\text{sub}}$ ) of 400 °C. The inset represents the electron diffraction patterns for the Mn<sub>4</sub>N film. (b) and (c) show the same set of images as (a) with the  $T_{\text{sub}}$  of 450 °C and 500 °C, respectively.

**Figure 5.** (a) Measurement temperature dependence of longitudinal resistivity ( $\rho_{xx}$ ) and (b) transverse resistivity ( $\rho_{xy}$ ) for the Mn<sub>4</sub>N films fabricated with the substrate temperature ( $T_{\text{sub}}$ ) of 400 °C (red), 450 °C (black), and 500 °C (blue). (c) Relationship between transverse conductivity ( $\sigma_{xy}$ ) and longitudinal conductivity ( $\sigma_{xx}$ ). (d)  $T_{\text{sub}}$  dependence of residual resistivity ( $\rho_{xx}^0$ ) and residual transverse conductivity ( $\sigma_{xy}^0$ ).

**Figure 6.** Replot of various measurement data against coercive field ( $H_c$ ).

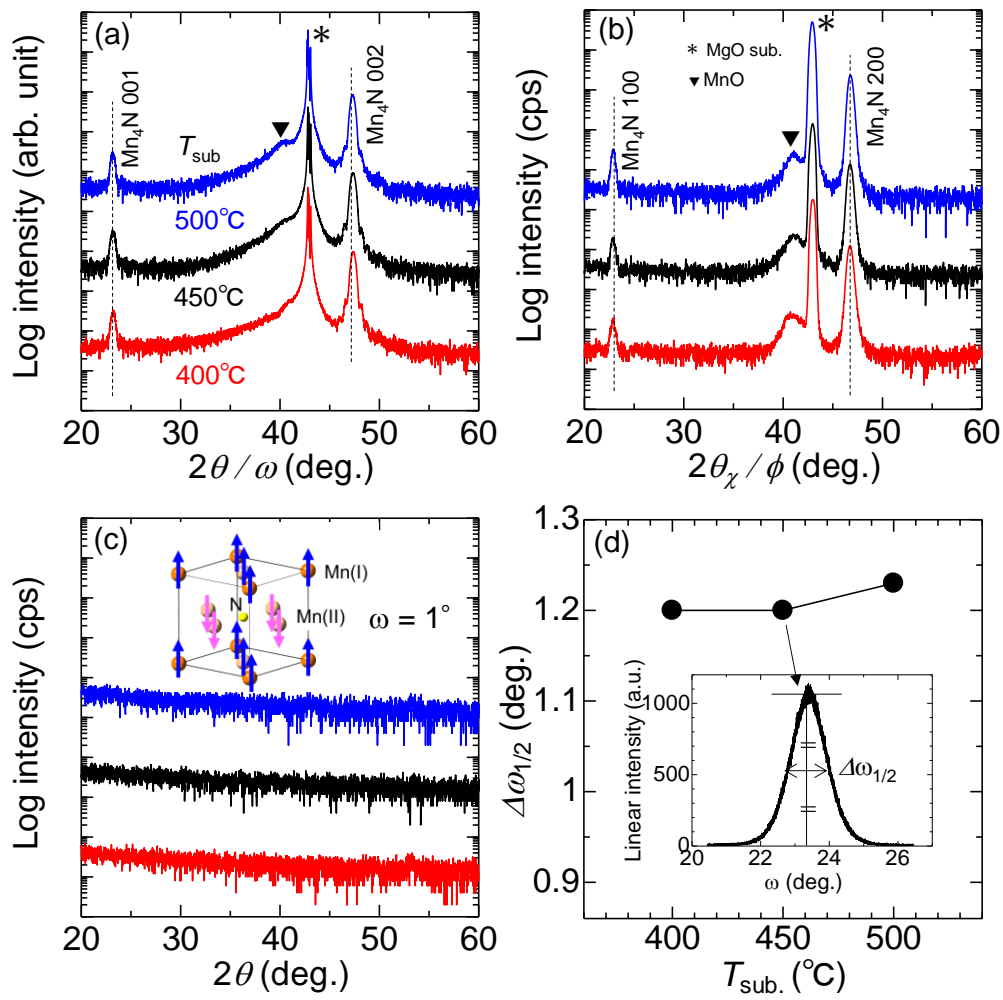


Fig. 1

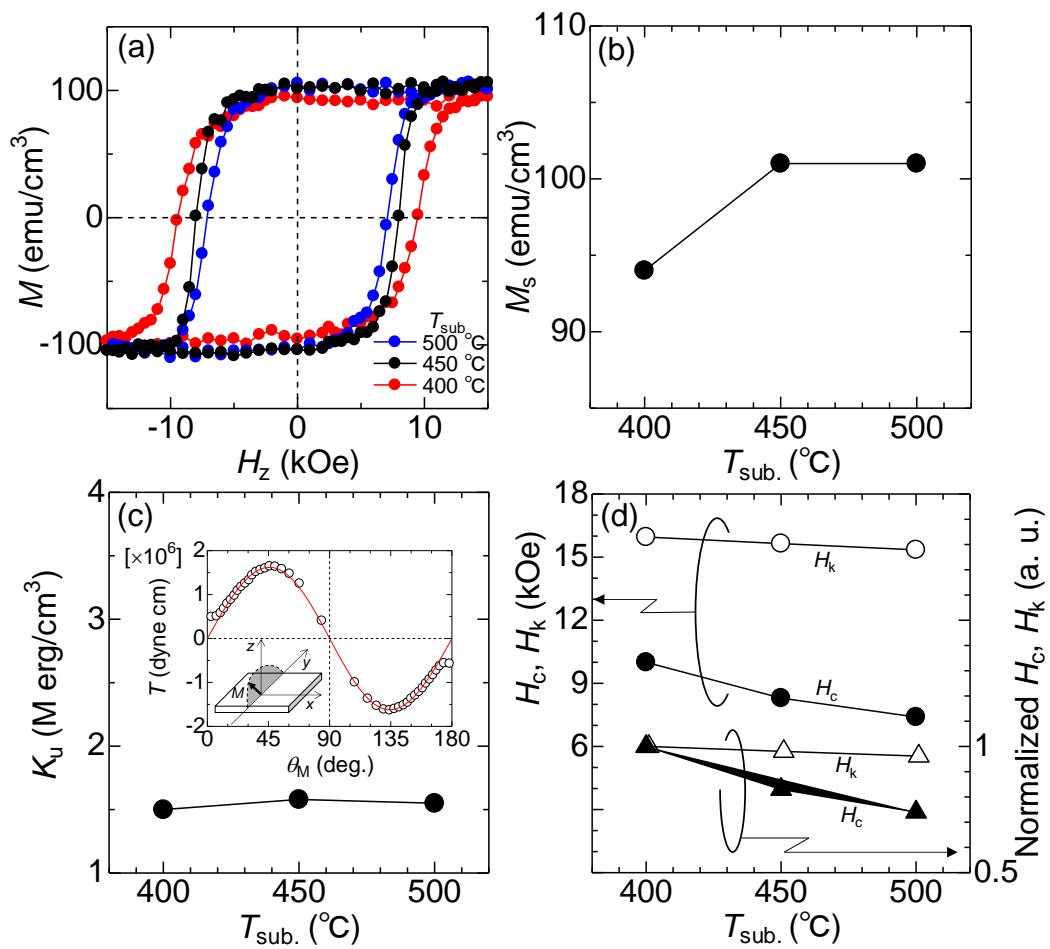


Fig. 2

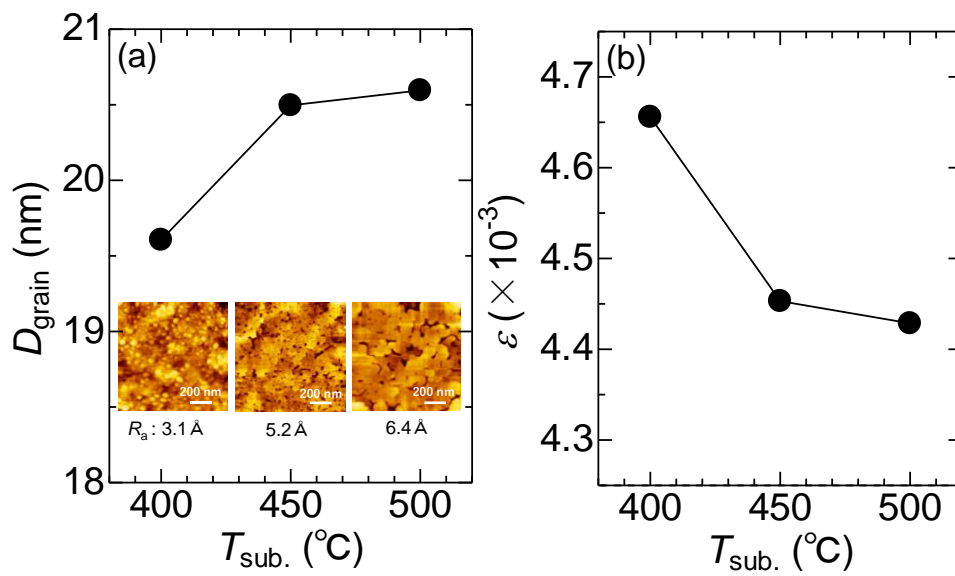


Fig. 3

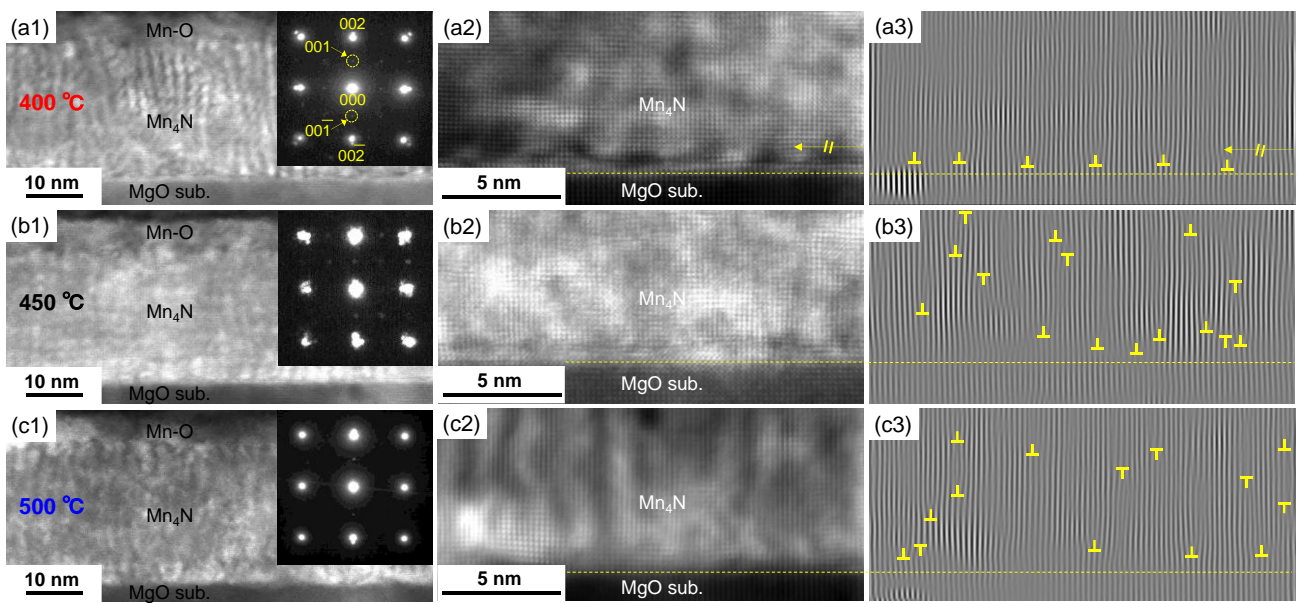


Fig. 4

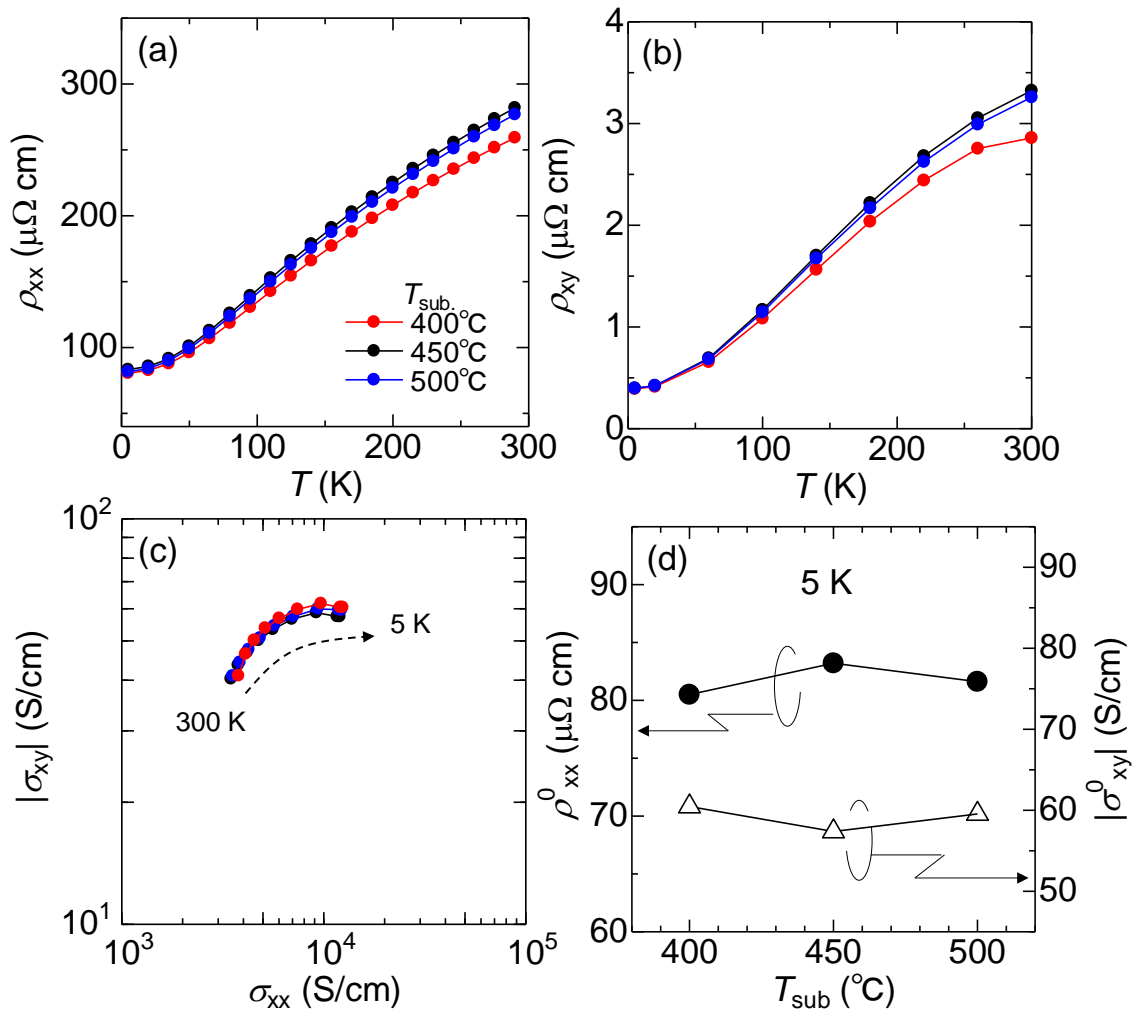


Fig. 5

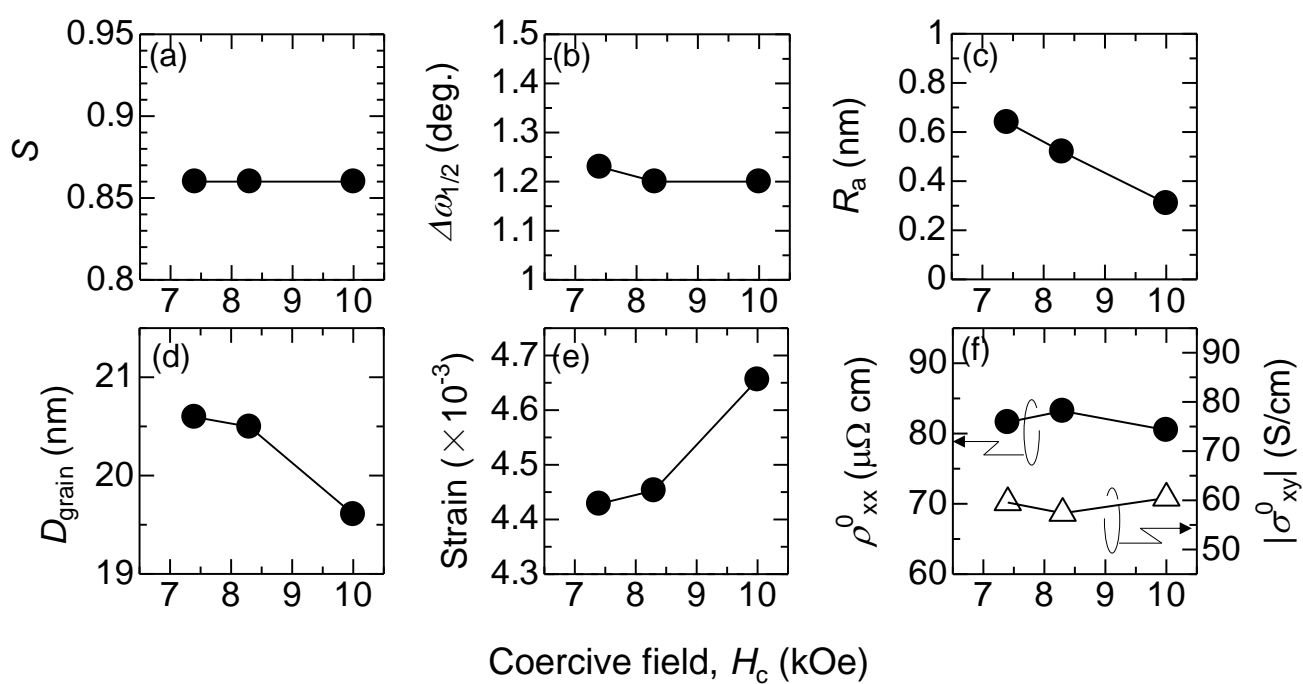


Fig. 6